ELSEVIER

Physica D 123 (1998) 183–205

PHYSICA D

Power-law singularities in gravity–capillary waves

J. Errett Hogrefe [a], Nicholas L. Peffley [a,b], Christopher L. Goodridge [a], William T. Shi [a], H. George E. Hentschel [a], Daniel P. Lathrop [a,b,*]

[a] Department of Physics, Emory University, Atlanta, GA 30322, USA
[b] Department of Physics, University of Maryland, College Park, MD 20742, USA

Abstract

Strongly driven waves break and lead to local singularities. Parametrically forced standing waves (Faraday waves) may break leading to a local power-law divergence on the free surface. We experimentally explore this state for its local structure, time dynamics and threshold for creation. A local analytical model for the surface height compares favorably with image sequences taken of individual events. Copyright © 1998 Published by Elsevier Science B.V.

1. Introduction

In this paper we explore singularities occurring on liquid surfaces as a consequence of overdriven standing waves. The singularities we are referring to are local divergences in the amplitude or gradients of some physical field. Many spatio-temporal dynamical systems exhibit singularities. These physical systems usually have some ultraviolet cutoff terminating the singularity at its tip. These cutoffs are extra physical phenomena which often come into play only when the ordinary description breaks down.

As an example, consider incompressible turbulence. Sreenivasan [1] and others observed that large fluctuations in the derivatives occur and that the dissipation field appears multifractal (a set of nested singularities). These singularities or near-singularities are cutoff in physical turbulent states by several possible phenomena, including a viscous cutoff of the small-length scales (Kolmogorov scale cutoff). The viscous cutoff is included in the Navier–Stokes formulation of fluid flow.

This first cutoff should be contrasted with one other mechanism– cavitation [2,3]. Large fluctuations in the velocity derivatives, often in the form of large-vorticity fluctuations, cause corresponding fluctuations in the pressure field. Large negative fluctuations in the pressure are given a cutoff by the formation of vacuum or vapor bubbles (cavitation bubbles) in the liquid. This formation falls outside the limited mathematical description of fluid flow – the Navier–Stokes equations. Large positive fluctuations in the pressure do not have as straightforward a cutoff, and the pressure fluctuations can reach enormous levels, enough to damage solids or possibly to cause light emission (cavitation luminescence and sono-luminescence).

Nonlinear optical systems exhibiting a positive Kerr coefficient also exhibit self-focusing and nonlinear propagation effects [4]. This may lead to the collapse of the optical power density into local divergences. This phenomenon has important consequences to optical damage of optical fibers and laser systems.

---

[*] Corresponding author. E-mail: dpl@complex.umd.edu

0167-2789/98/$19.00
PII S0167-2789(98)00120-1

These systems are often modeled in some simple situations by the nonlinear Schroedinger equation. This equation is known to have finite time singularities associated with self-focusing. The optical damage to real materials, as well as to some dispersive phenomena, produces limitations in the local power density, i.e., a small-scale cutoff.

Near-singularities have been studied in the complex Ginzberg–Landau equations. Luce and Doering [5] have studied this problem from the point of view of that the nonlinear Schroedinger equation is the conservative limit of the complex Ginzberg–Landau equations. As the former show finite time singularities, the way in which the dissipative case admits a small-length scale cap on the singularities (again an ultraviolet cutoff) proves interesting.

Gravitational singularities from another less understood example [6]. The formation of black holes and the possibility of naked singularities occurring during their formation constitute a hard-to-observe but tantalizing possibility. The governing equations – the Einstein equations – are a set of coupled nonlinear partial differential equations (PDE's) for the curvature and energy density. What classes of singularities these equations admit is not completely understood, but particular examples are known.

These systems appear to form a non-trivial list of diverse examples with one common feature: all spring from nonlinear PDE systems. Therefore, it appears useful to define a class of solutions of nonlinear PDE systems that exhibit local singularities or near-singularities and to study that group as a class.

Wave-breaking states necessarily contain singularities, since they exhibit a change from a simply connected free surface to a free surface connected in multiple ways. Singularities in surface waves occur in several contexts. The breaking of waves on a beach causes topological changes: the creation of spray, air entrainment, and foam. Breakers on a beach also have a large range of length scales in the gravity-dominated regime.

Waves on the open ocean that break can also show several types of singular phenomena. The limiting case of Stokes waves shows infinite acceleration. The spray and foam produced in deep-water breaking also contain gravity–capillary singular phenomena associated with the change in topology. This type of spray production also occurs in rivers and streams with significant surface and bulk turbulence.

The nature of these singularities has recently been the subject of several important theoretical works [7–10]. Wave-breaking singular phenomena in the ocean usually involve propagating waves and thus are difficult to disentangle from wind-driven properties and the convective instabilities involved.

All these natural phenomena did not adequately prepare us for the experimental observations of these singularities, which show not only large accelerations and velocities but large displacements as well. This type of singularity is perhaps more akin to phenomena observed in wave impact on cliffs. Impact of solid objects into bodies of water also may lead to similar phenomena. This we will explore in the section on the local behavior of the singularities.

In our experiments, surface wave singularities are produced on a liquid surface by vertically oscillating a container (Faraday excitation). Standing waves produced in this way can be precisely controlled, and they afford detailed local diagnostics for their time recurrent phenomena. These liquid singularities are modest in length and time scales, thus permitting a more complete experimental characterization than is possible for the other types of physical phenomena discussed earlier. In these experiments, the flat surface becomes unstable to periodic surface waves at a critical acceleration (via the Faraday instability [11]). As the excitation increases past periodic waves and modulated waves, a sharp transition to a state with spikes on the surface that eject droplets from the tip is observed. Much is already known about the onset of periodic surface waves and the existence of spatial and temporal chaos in this system [12–18].

Longuet-Higgins may be the first to have observed surface singularities arising from parametrically forced waves. Unfortunately, his analytical solution presented in that work is of the wrong concavity (concave down), and thus does not explain the observed phenomena.

Closely related work has been performed by Eggers, Brenner, Nagel, and their collaborators at the University of Chicago. These papers include a local analysis of the breakoff of a pendant droplet, and they find rich structure in that singularity. The singularity predicted by the analysis is of square-root form (height depending on radius as $h \sim r^{1/2}$). This type of singularity, as well as those found analytically by Kuznetsov et al., are weak-type singularities. Derivatives may diverge, but the form shows bounded height. Strong singularities, those with divergent amplitude (as the NLSE show), appear to exist in the surface wave problem. In their conclusion, Kuznetsov et al. described observations of "more powerful singularities observed in numerical experiments". As any physical system must show some upper bound (an ultraviolet cutoff), this is one issue we must address in our experiments. It appears that the Rayleigh instability (breakup of a thin neck into droplets) supplies that cutoff.

Bertozzi and Brenner have explored the types of singularities to be found in the two-dimensional surface flow limit, particularly the Hele–Shaw problem. They have found several types of singularities that depend sensitively on the initial conditions and that are difficult to resolve with full precision numerical simulations.

Finally we should mention the paper by Newell and Zakharov [9] which predicted a change in topology in gravity–capillary waves at a well-defined threshold for power injection. This prediction was based on analysis founded in Kolmogorov spectra for wave turbulence. It was their paper that stimulated our work described here.

We conjecture that we have observed a type of strong singularity on a free surface where the height of the surface diverges in the large viscosity limit. In this limit the droplet breakoff is delayed, removing the ultraviolet cutoff. This phenomenon is closely related to the theoretical predictions of Eggers [19] and Zakharov [20] of the existence of self-similar surface forms near a singularity.

This paper focuses on three aspects of ejecting surface waves. First, we pursue local models for the spatial and temporal structure of the singularity, including a self-focusing mechanism and the power-law form for the singularity. Second, we investigate the time dynamics of states exhibiting singularities. Finally, we determine the parameter values needed to cause a state with singularities, including the determination of the threshold value of the forcing and the form of testable models for that dependence.

2. Local characterization of the singularity

The Faraday singularity is produced by parametrically forcing a tank partially filled with liquid in the vertical direction. Small-amplitude periodic forcing of a bulk liquid predictably results in an observable periodic behavior of the free surface [11]. A forcing frequency can be chosen to excite the (2, 2) Fourier mode. This mode has one central maximum alternating in time with a central minimum. This central maximum sets the location for the ensuing singularity.

Fig. 1 shows a series of images from a high-speed movie of the events preceding and following the surface singularity in the Faraday experiment. In these images, the dark portion is created by refraction at the interface between the liquid and air and thus outlines the shape of the waves on the free surface. Fig. 1(a) shows the surface wave maximum that directly precedes the singularity. Interestingly, the height of this surface wave must be within a very specific range (the critical height was found to be about 7.0 cm) [21] in order to produce a singular event. If this surface-wave maximum is much taller, there is no ejection! Instead, its collapse results in the liquid's entraining an air bubble [22] – a dissipative process – followed by a smooth wave of very small height. Conversely, if the surface wave is not tall enough, the result is simply another smooth surface wave of greater height (gaining energy from the parametric forcing). Through this process of gradual amplification of surface waves, a surface wave of critical height, like the one in Fig. 1(a), can be produced. Photographs (b) and (c) show what happens after the maximum in (a) falls: a depression results in the free surface. This depression, with nearly cylindrical side walls, quickly collapses due to the pressure difference across the air–liquid interface. This collapse is responsible for the thin jet ejecting from the surface in Fig. 1(d), as well as its subsequent growth in (e)

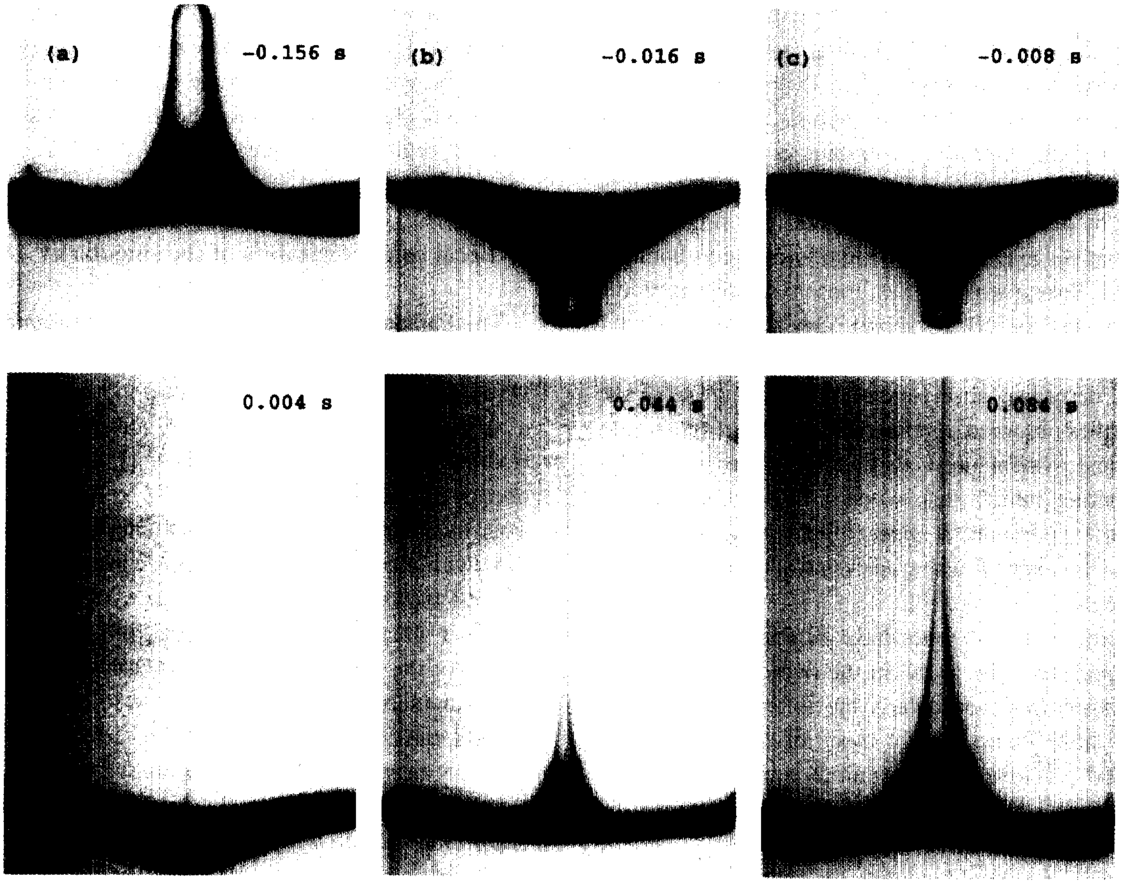

Fig. 1. Several images of the Faraday experiment were taken using a high-speed motion picture camera at 250 frames per second. These images illustrate the events around a singularity. (a) The last smooth wave (b) collapses, 9c) forming a cylindrical cavity that (d) quickly results in a surface singularity that in turn (e) and (f) grows due to the balance of inertial and surface forces.

and (f). Rayleigh instabilities in the growing spike result in droplet formation near its apex. Gravitational forces eventually cause the fluid in the spike to fall and rejoin the bulk liquid, leaving behind an elongated fluid structure that also breaks into droplets [7,23]. Inertial and surface forces are responsible for the growth of the singularity, whereas gravitational forces are responsible for its eventual demise [24].

Here we explore a local hydrodynamic model for the Faraday singularity as motivated by experimental observations. Figs. 1(b) and (c) show a collapsing cylindrical depression in the fluid surface. The model presented attempts to quantify how a collapsing cylinder can produce a surface singularity (d) as well as the early growth (e) of the singularity. The first step is to estimate the velocity field just before t_0 and, with the aid of a Taylor expansion and the Navier–Stokes equations, just after t_0, the time at which the singularity occurs. Surface tension is ignored in the Navier–Stokes equations. Next, we find the effect of the velocity field on the surface, $h(r,t)$, by examining the kinematic surface problem. Last, we verify that $h(r,t)$ is consistent with the velocity field that produced it by examining the Bernoulli equation, in which surface tension is included.

Several energies inherent to fluid motion are useful in characterizing the behavior of the fluid: kinetic energy, energy lost to friction over a given time interval (viscous power loss), surface tension energy, and gravitational energy. Analyzing the magnitude of these

Table 1
Expressions for various energies per unit mass

Energy per unit mass	Quantity
Interval	$v^2/2$
Viscous	$(\Delta t)\nu v^2/r^2$
Surface tension	$\sigma/r\rho$
Gravitational	gh

energies near the singular event is helpful. Table 1 lists the various energies per unit mass of fluid. Here, Δt is the characteristic timescale, r is the characteristic length of scale, and v is the local velocity of the fluid. The following fluid parameters also appear in the table: ν is kinematic viscosity, σ is surface tension, and ρ is density. Lastly, g is acceleration due to gravity. Near the singular event, Δt is small, r is small, v is large, and $v^2/2 \gg gh$. Therefore, inertial energy and surface energy are the important factors in the growth of the singularity. Over sufficiently small time intervals, very little of the total energy has been converted to heat by the viscous forces. Thus, to a good approximation, gravitational and viscous effects can be neglected when investigating the behavior of the fluid local to the singular event.

Consider as a simplified model of the self-focusing the problem of a collapsing cylindrical vacuum cavity of radius $R(t)$ in an ideal, incompressible fluid. This is motivated by the observations of the Faraday experiment (Figs. 1(b) and (c)) that suggest that the air cavity directly preceding the singularity is cylindrical in shape. What is the resulting behavior of the free surface after the cylinder has collapsed? If the velocity field of the bulk liquid has only a radial component that varies only with r, incompressibility of the fluid $\nabla \cdot \mathbf{v} = 0$) requires that $v_r(r)$ be described locally by $v_r = -c/r$ where r is the radial cylindrical coordinate and c is a positive constant. By solving this differential equation for the position of the cylindrical wall $R(t)$, one finds that the radius of the cylinder collapses as $R(t) \sim \sqrt{t_0 - t}$. As the radius of the cylinder approaches zero, a singularity occurs because (1) the fluid impacts itself and (2) the velocity diverges as R, r approach zero. At $t = t_0$, the time of impact, a filament of high pressure must arise to decelerate the fluid along $r = 0$. This pressure enforces incompressibility. Since the fluid cannot pass through itself, the radial velocity must obey $v_r = 0$ for $t \geq t_0$. The only relief from this pressure is for the fluid to escape toward the free surface along the liner $r = 0$. Thus, the effect of the pressure near the singularity is to modify the assumed $v_r = -c/r$ to a form such as $v_r = -cr/(1+r^2)$, so that the radial velocity v_r goes smoothly to zero at $r = 0$. Since the region of interest is in the neighborhood of the singularity, one can perform a Taylor series expansion of v_r near $r = 0$. Such an expansion reveals a vanishing zeroth-order term and a first-order term of $v_r \sim -r$. Incompressibility requires that $\nabla \cdot \mathbf{v} = 0$. Thus, the radial velocity $v_r \sim -r$ necessitates an axial velocity $v_z \sim z$. By inserting this velocity field spatial dependence into the Navier–Stokes equations

$$\partial_t \mathbf{v} + (\mathbf{v} \cdot \nabla)\mathbf{v} = -\frac{1}{\rho}\nabla P + \nu \nabla^2 \mathbf{v} \tag{1}$$

one finds that the time dependence for the radial and axial velocities are, respectively, $v_r = -ar/2(t - t_0)$ and $v_z = az/(t - t_0)$, where a is a unitless, real constant that characterizes the magnitude of v. Appearing in these equations are the inertial terms on the left-hand side, and the pressure term and the viscous term on the right-hand side. Surface tension effects have not been used explicitly here, but would be linked to the pressure field P by serving as a boundary condition for P. Gravitational effects are neglected since they are small in comparison to inertial and surface forces for times near $t = t_0 \equiv 0$. In arriving at these velocity components, the divergence of the above Navier–Stokes equations is taken, leaving Poisson's equation for $P : \nabla^2 P \sim -\rho \nabla \cdot (\mathbf{v} \cdot \nabla)\mathbf{v}$. Assuming that the pressure varies only with r, one can solve the one-dimensional Poisson equation and obtain an expression for P that can be used at last to obtain the velocity components.

With this information about the velocity field near the singularity, one can begin to answer the central question: what is the effect of this collapsing cylinder on the free surface? Answering this question involves solving the PDE for the kinematic surface problem

$$\partial_t h + v_r \partial_r h = v_z|_{z=h}. \tag{2}$$

By substituting the earlier expressions for v_r and v_z, this differential equation can be solved for $h(r,t)$ using the method of characteristics. The solutions have the form

$$h(r,t) = t^{\alpha} f(rt^{\beta}). \tag{3}$$

There are two types of solution for the function $h(r,t)$. If $\alpha = a$ and $\beta = a/2$, then the function f is arbitrary. The second solution, however, is

$$f(u) = u^{\gamma} \tag{4}$$

where $u = rt^{\beta}$ and $\gamma = (a-\alpha)/(\beta - a/2)$; at this point α and β are arbitrary. (Zakharov also derived homogeneous solutions but for a two-dimensional Cartesian system [20].) This leads naturally to the question of which power law for u is selected, as different power laws are represented by different choices of α and β. To address this exponent selection the effect of the surface on the velocity field must be examined. This verifies that the model is self-consistent. Recall that by employing the kinematic surface equation, one can use the velocity field v to obtain a general form for h. Now, one checks which specific solution of h is consistent with v by examining the Bernoulli equation governing an inviscid fluid. (Viscous effects are neglected since very little energy is dissipated over the small time interval $\Delta t = t - t_0$. This assumption of minimal energy dissipation is supported in our model velocity field $\mathbf{v}$ which yields $\nabla^2 \mathbf{v} = 0$; i.e., $\mathbf{v}$ is a frictionless field.) Inertial and surface tension terms are included; by introducing the surface tension term explicitly here, one derives new information about the solutions for h. As before, the gravitational term is neglected since its effect at early times is small in comparison to the included terms. Assuming an irrotational flow, the Bernoulli equation governing the velocity potential $\mathbf{v} = \nabla\phi$ at the free surface is

$$\partial_t \phi + \frac{1}{2}(\nabla\phi)^2 + \frac{\sigma}{\rho} r^{-1} = 0. \tag{5}$$

Note that we have selected only the small principle radius of curvature and have neglected the larger one in the term $(\sigma/\rho r_1 + \sigma/\rho r_2)$. This is reasonable for a thin jet, and neglects the Rayleigh instabilities associated with the other radius. Substituting the velocity potential $\phi = az^2/2t - ar^2/4t$ corresponding to our $\mathbf{v}$ and focusing on the region vertically up in the singularity ($z \gg r$), all remaining terms are satisfied for the solution with a particular exponent $f(u) \sim u^{-1/2}$. This analysis yields a predicted growth of

$$h(r,t) = btr^{-1/2}, \tag{6}$$

where $b = \sqrt{2\sigma/\rho a(1-a)}$ is a constant related to the amplitude of the singularity and is obtained by matching terms in the Bernoulli equation. If b is to be real, then the positive constant a, which characterizes the magnitude of the post-singularity velocity field, is restricted to be in the interval (0, 1).

If the solutions have the form $h = bt^{\alpha}(rt^{\beta})^{\gamma} = btr^{-1/2}$, then α and β should obey the relation $\alpha = 1 + \beta/2$ for *any* particular choice of α or β. This relation is necessary and sufficient to characterize any fit to experimental data as a successful fit. If this relation is not satisfied in the process of scaling experimental data, then the theory is not valid and does not accurately model the experiment. Also noteworthy is that the theory makes no allowances for particular choices of α or β; an entire family of values is predicted.

In the development of this theory, the effects of gravity and the effects of Rayleigh instabilities high in the vertical neck of the spike have been neglected. The characteristic velocity due to gravitational effects is $v_{zg} \sim gt$. The result $v_z \sim z/t$ was found for regions local to the singularity. Thus, by equating v_{zg} and v_z, one finds for any fixed time t a boundary for z below which gravitational effects are important: $z \sim gt^2$. The timescale for droplet breakup due to Rayleigh instabilities in a cylindrical jet of radius r_R is given by $t \sim 6\nu\rho r_R/\sigma$ [25]. A radial dependence of $r \sim b^2 z^{-2} t^2$ was predicted by theory. Hence, by equating r_R and r in the two previous equations, one finds for any fixed time t a boundary for z above which Rayleigh effects should dominate: $z \sim \sqrt{6\nu b^2 \rho t/\sigma}$. Fig. 2 shows these two boundaries with actual data from the Faraday experiment appearing as a series of vertical lines.[1] The

---

[1] In every plot in this section containing a spatial or temporal variable, each spatial variable is in centimeters, and each temporal variable is in seconds.

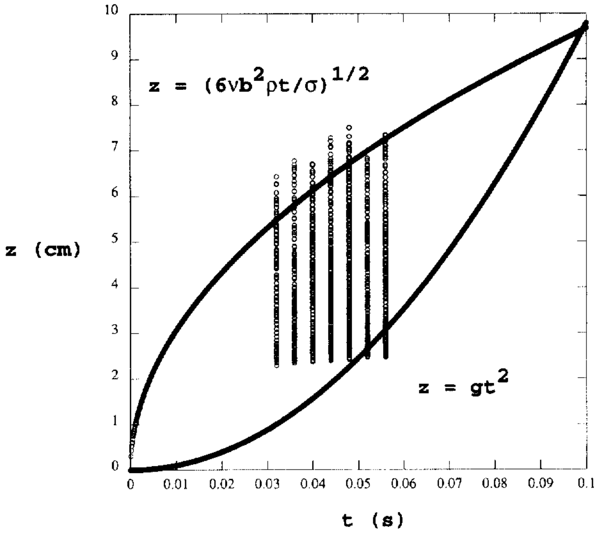

Fig. 2. The region between the two boundary curves corresponds to the domain of validity of the theory. Below the lower curve, $z = gr^2$, gravitational effects are important. Above the upper curve, $z = (6\nu b^2 \rho t/\sigma)^{1/2}$, Rayleigh instabilities dominate. The circles indicate experimental data used in the analysis.

region between the two boundary curves is the region in which this theory is expected to hold.

Most of the data fall within the domain of validity, even though the top curve is a conservative estimate of the least upper bound. Rayleigh instabilities are associated with a stationary, cylindrical fluid structure. Observations suggest that our non-cylindrical jet not only convects any developing local instabilities far away from the region of interest quickly, but does so with shearing (the topmost fluid rises faster than the bottommost fluid). The following explains in greater detail why the upper curve is merely an estimate for the least upper bound and why we think that this estimate is a conservative one. The Rayleigh instability causes the local singularity to break up into droplets high on the thin neck. Our understanding of this process has come from a simple application of the theory of breakup of fluid cylinders due to surface tension in the presence of viscosity [25]. This theory is not purely applicable to our case due to two differences in the fluid/surface configuration. First, our fluid structure is not a cylinder, and the radius of the structure does depend on height. Our initial simple estimates of the time for the Rayleigh-based breakup have treated each radius just as a separate location of instability (as the radius varies slowly), and thus the timescale for breakup is dependent on height. This is obviously only an approximation. The second problem is perhaps more serious. Instabilities occurring on the neck of the fluid are both convected vertically upward by the axial velocity and stretched. As $\partial v_z/\partial z$ is positive, stretching will affect instabilities on the surface in a severe way. Any surface perturbation that is growing will have its wavelength grow in time (stretched). This complication makes the simple linear stability analysis based on Fourier modes inapplicable. The Rayleigh instability in the presence of stretching has not been researched in detail.

2.1. Faraday experiment

2.1.1. Description of experiment

A general description of the Faraday experiment has already been given (see Fig. 1 and surrounding text). However, the specifics of the experiment which were neglected earlier are discussed here.

The tank containing the fluid was 12 cm × 12 cm in the horizontal plane and 28 cm tall. About 1.00×10^3 cm^3 of fluid, a 92%-glycerin 8%-water mixture with a viscosity of about 300 centistokes and a surface tension of 64.9 dyne/cm, were put into the tank so that the fluid depth was 7.0 cm. The tank was shaken at a frequency of 7.40 Hz. This frequency was chosen to excite the (2, 2) Fourier mode of the tank so that surface maxima and minima appeared conveniently in the center of the tank. The peak acceleration of the tank was 5.2 m/s^2. (Note that periodic accelerations less than one gravity may produce these singularities.)

The singularities on the liquid–air interface were filmed using a high-speed camera. Lights were focused on a white background placed behind the tank; no direct light from the sources illuminated the fluid. Underneath and to the sides of the tank was a black cloth which served to contrast the liquid–air interface (dark) against the background behind the tank (light). A high-speed camera capable of filming 250 frames per second equipped with a 50 mm lens was placed about 5 m from the tank so that the aperture was level with respect to the horizontal plane, and was aimed at the stationary horizontal fluid–air interface.

Once the tank was set in motion, the periodic motion of the tank produced a singularity or near-singularity on the surface of the fluid approximately once every 14 oscillations. (The timescale for the growth of the singularity is smaller than the timescale for the shaking itself.) Because of the aperiodic nature of this state (see Section 3), events closer and further from the critical height can be observed. The ejection states of interest were those characterized by a very thin, exactly vertical filament of fluid that shot up from the surface as a result of the collapse of the previous smooth wave of critical height. The filming process would often take between 15 and 30 min before a singularity that matched all the criteria was recorded. Filming sessions never lasted longer than 30 min because both the lights and the motion of the tank caused the fluid to heat up and thereby lower its viscosity. Care was taken to switch off the lights between filming periods so that temperature variations were minimized. The black-and-white images were transferred to and saved on a computer where all the analysis was done.

2.1.2. Experimental results

The theory for the development of the singularity predicted the power-law scaling

$$z = bt^{\alpha}(rt^{\beta})^{\gamma} = btr^{-1/2}. \qquad (7)$$

The predicted scaling demands that the following relation between the exponents α and β be satisfied by the experimental data

$$\alpha = 1 + \tfrac{1}{2}\beta \qquad (8)$$

and, further, that no particular (α, β) pair be inferred. Indeed, the results confirm the theory very well, as shown in Fig. 3 (see footnote 1).

The inset in Fig. 3 shows the r and z coordinates, i.e., the raw data, of the free surface singularity for the first few frames after t_0.[2] The earlier frames are nearer to the cylindrically symmetrical center. By plotting z/t^{α} versus rt^{β}, all the data collapse onto one curve as predicted. This curve, a power law for $u = rt^{\beta}$, is shown in the main portion of Fig. 3. The predicted scaling of $\alpha = 1 + \beta/2$ was used to generate this plot. But was this the best possible scaling?

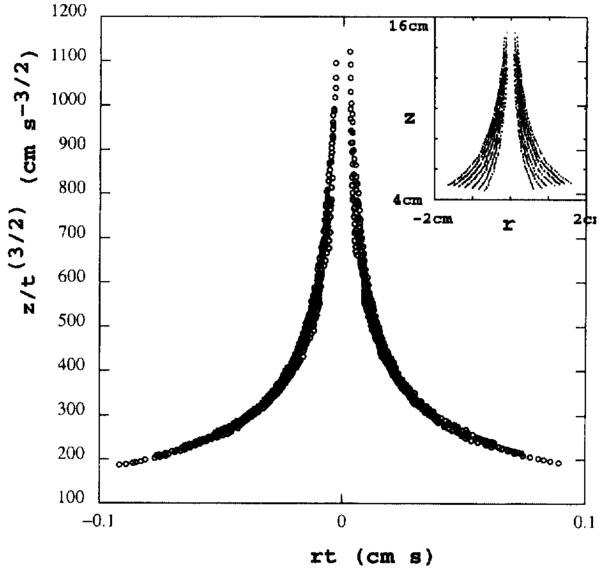

Fig. 3. Data from the Faraday experiment are shown. (a) The inset shows the growth of the surface singularity for different times < 0.06 s after t_0. (b) The main graph shows a collapse of the data in the inset according to the scaling $\alpha = 1 + \beta/2$ and the choice $(\alpha, \beta) = (3/2, 1)$.

The answer to that question is very nearly "yes". A statistical test of collapse for (α, β) pairs is given by the statistical coefficient of determination R from the linear regression for Fig. 5; R is defined in the interval [0, 1]. Fig. 4 is an image in which different colors represent different intervals of these R values for (α, β) pairs between $\alpha = [-1, 1]$ and $\beta = [-1, 1]$. Colors near red indicate better fits; colors near blue indicate poorer fits. This plot of coefficients of determination in Fig. 4 thus highlights the line that best fits the experimental data. This line, $\alpha = 4/5 + \beta/2$, is shown in white. The line predicted by theory and represented in Fig. 3, $\alpha = 1 + \beta/2$, is shown in black. The two

---

[2] Technically, all figures in this section involving r and z actually show the Cartesian coordinates (x, z) representative of a cross-section of a cylindrically symmetrical shape centered at $x = 0$. However, because the shape is cylindrically symmetrical, thinking of the x-coordinate in terms of a radius is convenient. "Negative" radial values are plotted so that the shape of the singularity is preserved in the presentation.

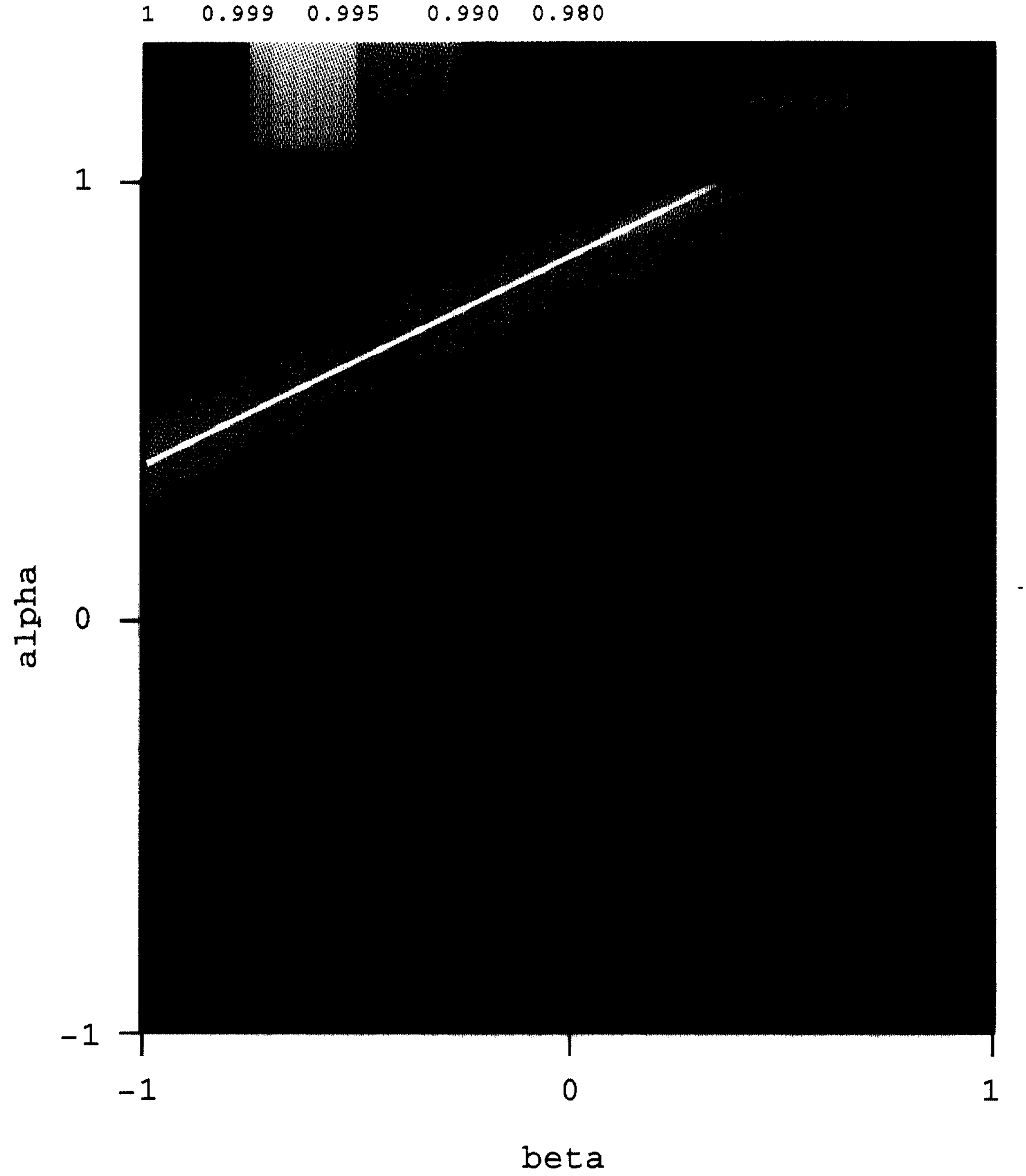

Fig. 4. The collapse of data for Faraday singularities is shown. Coefficients of determination for many (α, β) pairs are represented by colors. These colors are shown in the legend: red represents the interval $R = [0.999, 1]$, yellow represents the interval $R = [0.995, 0.999)$, green represents the interval $R = [0.990, 0.995)$, and so forth until blue which represents the interval $R = [0, 0.980)$. The white line is the line that best fits the experimental data: $\alpha = 4/5 + \beta/2$. The black line is the line predicted by theory: $\alpha = 1 + \beta/2$.

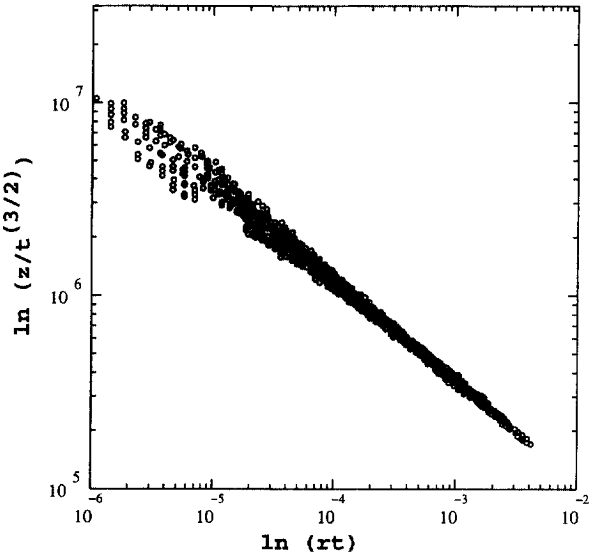

Fig. 5. For the Faraday experiment, a log–log plot of the collapsed data in Fig. 3 is shown. The slope of this line is $\gamma = -0.50$; the coefficient of determination is $R = 0.987$.

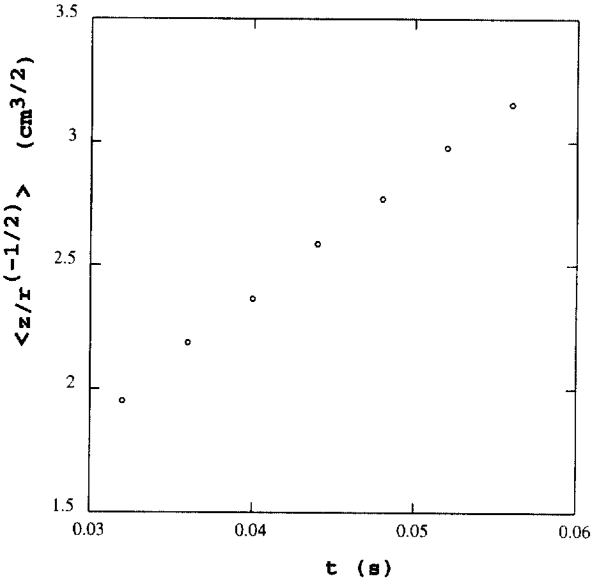

Fig. 6. For the Faraday experiment, average values of $z/r^{-1/2}$ for each snapshot are plotted against time. The coefficient of determination $R = 0.999$ indicates a linear behavior. The slope of this line gives $b = 50$.

lines are parallel and nearly coincide, indicating a reasonable match between theory and experiment. The (α, β) pair that was used to produce those three figures, $(3/2, 1)$, is a pair that shows a typical fit to the experimental data.

Fig. 5 shows a log–log plot of the data in Fig. 3. (The raw data were first folded about the line $r = 0$ in order that no logarithms of negative numbers were taken.) Again, the same $(\alpha, \beta) = (3/2, 1)$ pair for the predicted scaling is shown. The plot appears linear, just as predicted by the theory. Furthermore, the slope of this line is $\gamma = -0.50$, exactly the value $-1/2$ predicted by the theory. A slight scatter in the data results in a coefficient of determination of $R = 0.987$.

Fig. 6 shows a plot of the average value of $z/r^{-1/2}$ for each snapshot against time. (One snapshot is a set of (r, z) coordinates of the edge of the singularity at a specific time in the early growth phase of the singularity.) This plot of $\langle z/r^{-1/2}\rangle$ versus t results in a very straight line ($R = 0.999$). The precise fit to a line is another example of the close agreement between experiment and theory.

The slope of this line is $b = 50$. Recall that theory defines $b = \sqrt{2\sigma/\rho a(1-a)}$ as a constant characterizing the magnitude of the singularity, where a is a unitless constant in the interval $(0, 1)$ related to the magnitude of the post-singularity velocity field of the fluid. Apparently, by determining b one learns something about a without ever directly measuring the velocity field of the fluid. Solving the quadratic equation for a yields two solutions, $a = 0.04$ and $a = 0.96$. The smaller term is discarded since velocity fields of small magnitude presumably are not associated with large-surface singularities. That one can learn something about the velocity field of the singularity simply by quantifying its magnitude is a satisfying and useful result.

The Faraday experiment was repeated and its data were analyzed similarly several times. The figures shown were from a typical dataset.

2.2. Impact experiment

2.2.1. Description of experiment

The impact of a solid sphere of sufficient velocity upon the free surface of a liquid produces a surface singularity. Fig. 7 shows a series of images from a

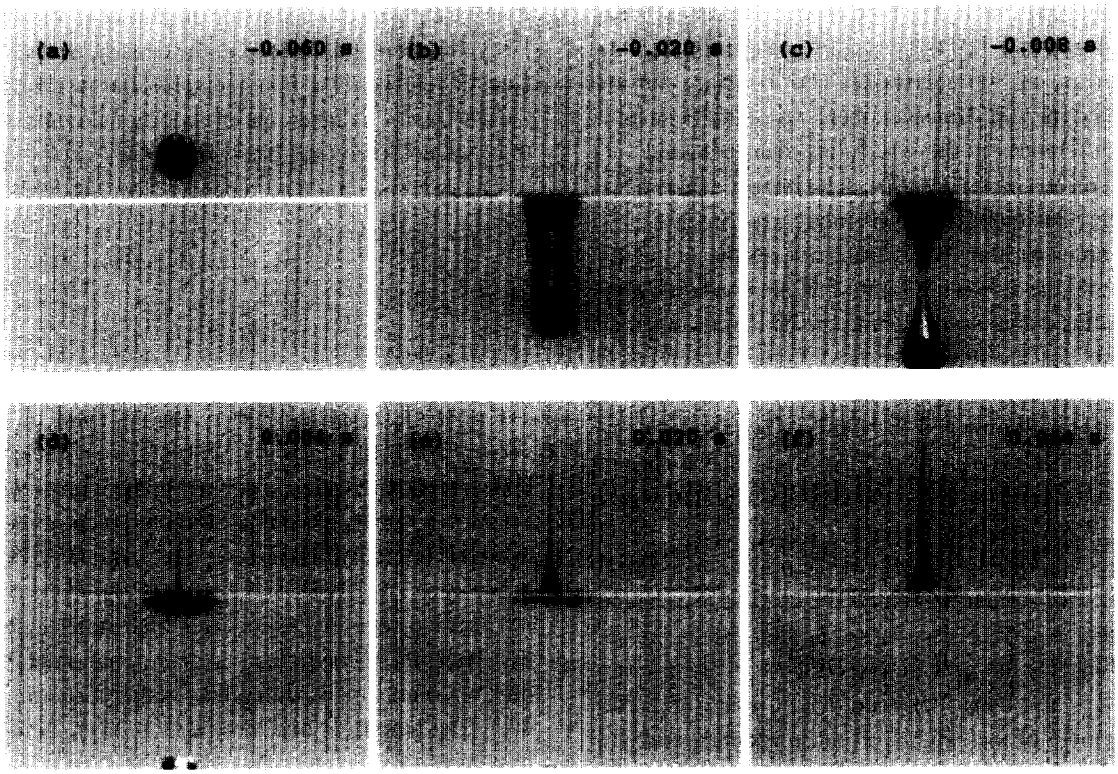

Fig. 7. Several images of the impact experiment were taken using a high-speed motion picture camera at 250 frames per second. (a) The metal sphere falls then impacts the surface leaving behind (b) a cavity that (c) pinches off and forms an hourglass-shaped structure, the collapse of which (d) quickly results in a surface singularity that, in turn, (e) and (f) grows due to the balance of inertial and surface forces.

high-speed movie of the events preceding and following the surface singularity. The dark portion is the interface between the liquid below and the air above. The photograph in (a) shows the ball directly before it impacts the surface. After the ball impacts the surface, it continues to fall through the fluid, leading behind a depression on the surface shown in (b). The depression seems cylindrical, as in the Faraday experiment, but only momentarily. The cylindrical depression shown in (b) is being stretched by the falling ball. In (c), the stretching cylinder is pinched off near its center, resulting in an hourglass-shaped depression. Note that the stretching cylindrical depression shown in (b) and the cylindrical depression associated with the Faraday experiment collapse quite differently. The hourglass-shaped depression quickly collapses, again due to the pressure difference across the air–liquid interface, resulting in the singular event shown in (d). The photographs in (e) and (f) show the subsequent development of the singularity. Similar to the Faraday singularity, Rayleigh instabilities in the growing spike result in droplet formation near its apex. The fluid in the spike falls and rejoins the bulk liquid, leaving behind an elongated "filament" of fluid that also breaks into droplets.

The impact experiment was designed to crudely model the Faraday experiment at least for times near t_0. The dropping of the ball simulates the collapse of the last smooth wave even though the mass distribution in each was very different. As many other common parameters as possible were matched: the diameter (1.11 cm) and dropping height of the ball (7.0 cm) in the impact experiment were chosen to coincide with the diameter and height of the last smooth wave in the

Faraday experiment. The fluid used in each experiment was identical: a 92%-glycerin 8%-water mixture with a viscosity of 300 centistokes and a surface tension of 64.9 dyne/cm. However, there were small unavoidable differences in the viscosities, densities, and surface tensions of the metallic ball (impact experiment) and the last smooth wave (Faraday experiment).

In order to film the singularities on the liquid–air interface, the following lighting techniques and camera settings were used. Behind the tank that contained the fluid was a white background. Lights were focused on the white background only; no direct light from the sources illuminated the fluid. A high-speed camera equipped with a 50 mm lens was used to record the events local to and including the singularity at a rate of 250 frames per second.

The Faraday experiment and the impact experiment appear very similar to the naked eye: each experiment produces a surface singularity. Similar forces are responsible for the growth and collapse of each structure. It is also clear, however, that at times long after t_0, the time of the singular event in each experiment, the Faraday experiment is markedly different than the impact experiment. Clearly, these differences are due to the differences between parametric forcing and impulse forcing. Therefore, any quantitative similarities between the two experiments would be at times very close to $t = t0$.

Upon investigation of the impact experiment, one finds that the impact of the ball produces a stretching cylindrical minimum in the fluid surface that pinches off, resulting in an hourglass-shaped minimum. Perhaps the differences in the Faraday and impact singularities are due to the differences in the collapses prior to t_0.

2.2.2. *Experimental results*

The results for the impact experiment also suggest power-law behavior. Since the theory for a collapsing cylinder does not apply to this experiment, one would certainly not expect solutions of the form $z = btr^{-1/2}$. However, the more general form of $z = bt^{\alpha}(rt^{\beta})^{\gamma}$ (the solution to the kinematic surface problem in the theory) seemed like an appropriate place to begin. Here, b is still a constant related to the amplitude of the singularity, but *cannot* be related to the density, surface tension, or velocity field. In other words, because the form $z = bt^{\alpha}(rt^{\beta})^{\gamma}$ is taken out of its original context and thus has no theoretical basis, $b \neq \sqrt{2\sigma/\rho a(1-a)}$.

The experimental data indeed follow the form

$$z = bt^{\alpha}(rt^{\beta})^{\gamma} \tag{9}$$

for the scaling

$$\alpha = \tfrac{2}{5} + \tfrac{2}{5}\beta. \tag{10}$$

Fig. 8 illustrates this fit. A log–log plot of z/t^{α} versus rt^{β} results in a line with some coefficient of determination R which is defined in the interval [0, 1]. Fig. 8 is an image in which different colors represent different intervals of these R values for (α, β) pairs between $\alpha = [-1, 1]$. and $\beta = [-1, 1]$. Colors near red indicate better fits; colors near blue indicate poorer fits. This plot of coefficients of determination in Fig. 8 thus highlights the line that best fits the experimental data. The empirical line, $\alpha = 2/5 + 2\beta/5$, is shown in white.

As in the Faraday experiment, no (α, β) pair falling on this line is appreciably better or worse than any other, and only times near t_0 follow the scaling. Experimental fits to the scaling $\alpha = 2/5 + 2\beta/5$ can be interpreted to mean that $\gamma = -2/5$ and thus

$$z = b(r/t)^{-2/5}. \tag{11}$$

Notice that this behavior is far different than the behavior of the Faraday experiment, even though in both experiments only times near t_0 were investigated! This surprising result is perhaps best explained by the differences in shape between the pre-singularity surface depressions: a cylindrical cavity corresponding to the Faraday experiment and a conical cavity corresponding to the impact experiment.

The inset in Fig. 9 shows the r and z coordinates, i.e., the raw data, of the free surface singularity for the first few frames after t_0 (see footnote 1). The earlier frames are nearer to the cylindrically symmetric center. By plotting z/t^{α} versus rt^{β}, all the data collapse onto one curve as mentioned earlier. This curve, a power law for $u = rt^{\beta}$, is shown in the main portion

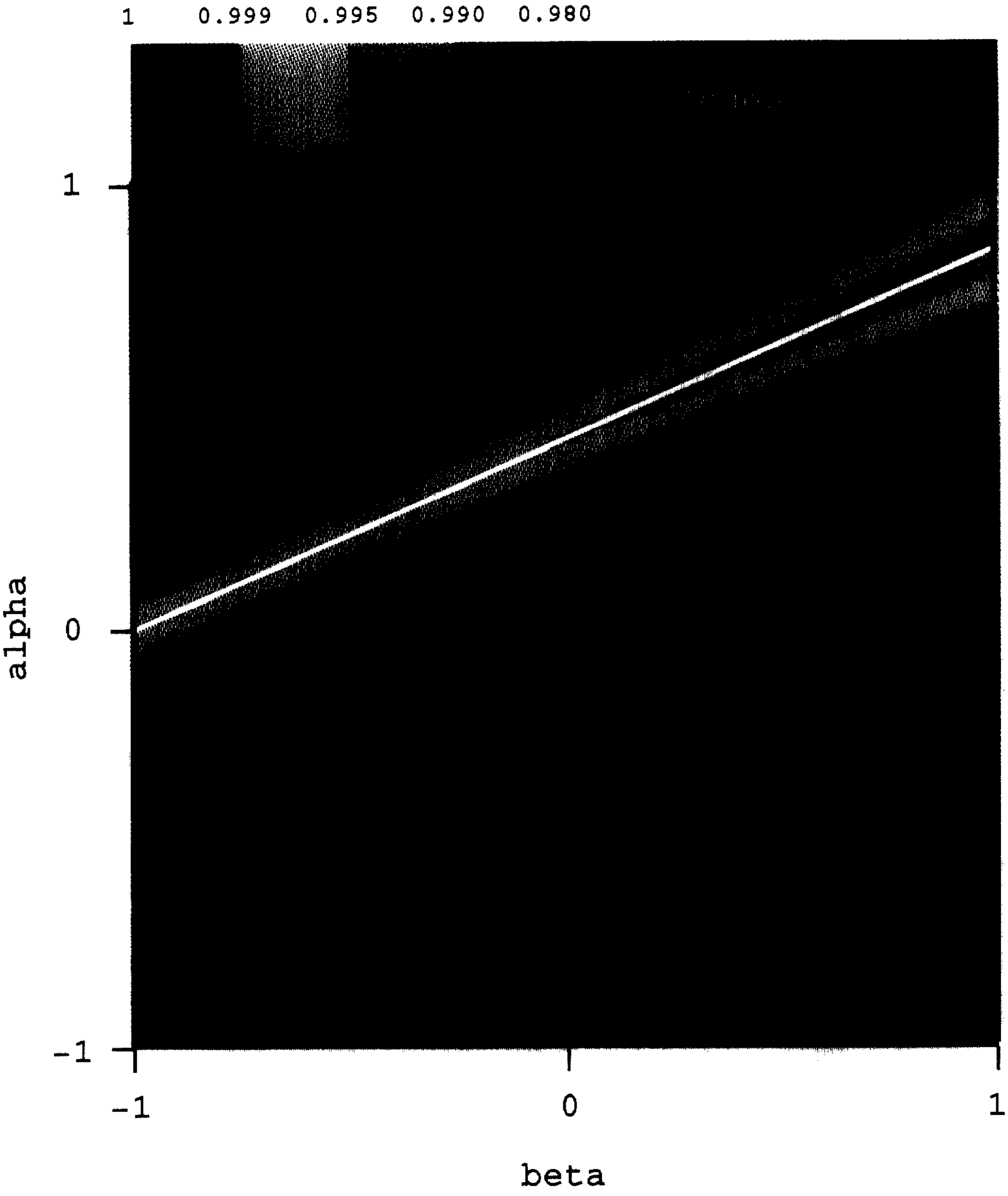

Fig. 8. The collapse of data for impact singularities is shown. Coefficients of determination for many (α, β) pairs are represented by colors. These colors are shown in the legend: red represents the interval $R = [0.999, 1]$, yellow represents the interval $R = [0.995, 0.999)$, green represents the interval $R = 0.990, 0.995)$, and so forth until blue which represents the interval $R = [0, 0.980)$. The white line is the line which best fits the experimental data $\alpha = 2/5 + 2\beta/5$.

of Fig. 9. The scaling $\alpha = 2/5 + 2\beta/5$ was used to generate this plot. Since no (α, β) pair following this scaling is better than any other, the arbitrary choice $\alpha = \beta = 2/3$ is shown for simplicity.

Fig. 10 shows a log–log plot of the data in Fig. 9 (see footnotes 1 and 2). (The raw data were first folded about the line $r = 0$ in order that no logarithms of negative numbers were taken.) The plot appears very

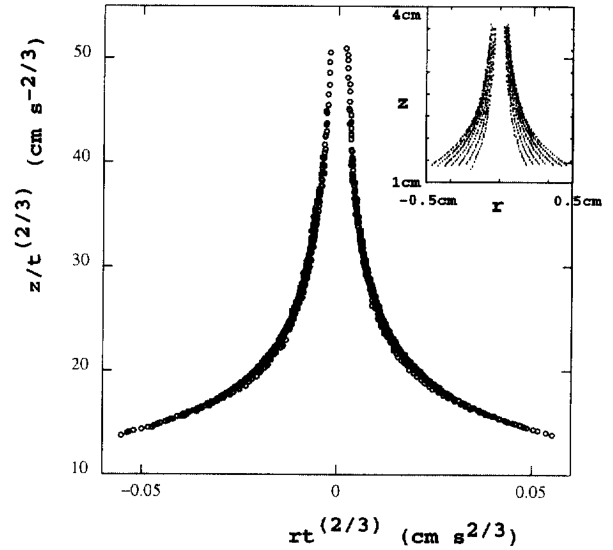

Fig. 9. For the impact experiment, (a) the inset shows the growth of the surface singularity for different times $< 0.06\,\mathrm{s}$ after t_0. (b) The main graph shows a collapse of the data in the inset according to the scaling $\alpha = 2/5 + 2\beta/5$ and the choice $\alpha = \beta = 2/3$.

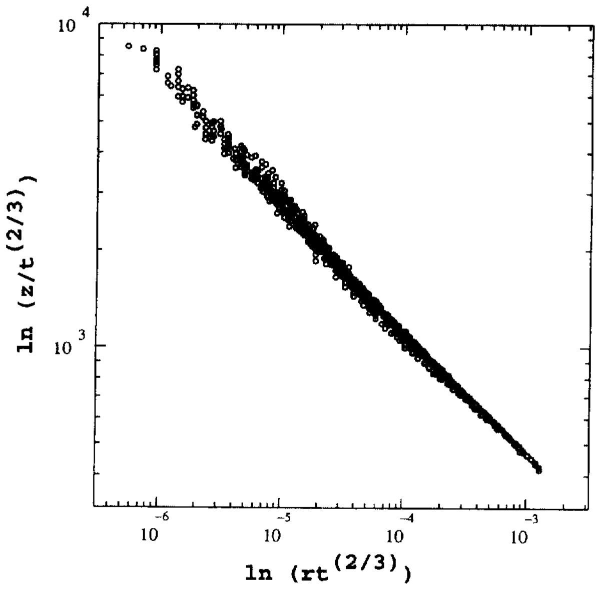

Fig. 10. For the impact experiment a log–log plot of the collapsed data in the previous figure is shown. The slope of this line is $\gamma = -0.40$; the coefficient of determination is $R = 0.995$.

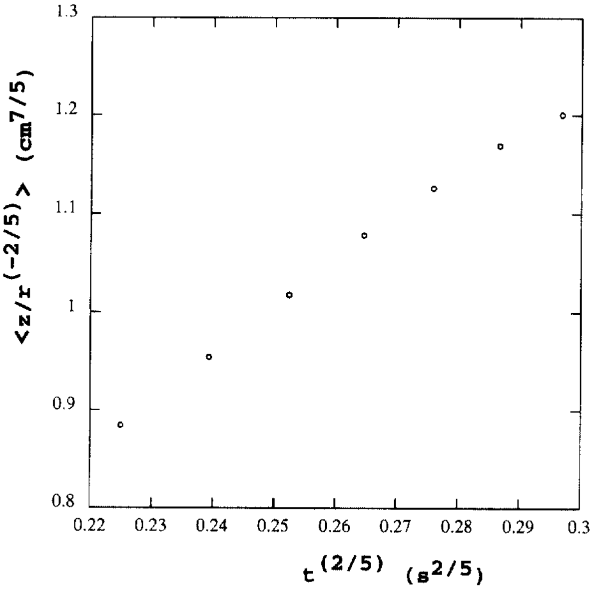

Fig. 11. For the impact experiment average values of $z/r^{-2/5}$ for each snapshot are plotted against $t^{2/5}$. The coefficient of determination $R = 0.995$ indicates a linear behavior. The slope of this line gives $b = 4.1$.

linear, which indicates a good fit to the scaling. The line has a slope of $\gamma = -0.40$ and a coefficient of determination $R = 0.995$.

Fig. 11 shows a plot similar to the one in Fig. 6, but for the solutions $z = (r/t)^{-2/5}$ (see footnote 1). The average values of $z/r^{-2/5}$ for each snapshot of the growing singularity are shown plotted against $t^{2/5}$. This plot results in an extremely straight line ($R = 0.995$), again indicating an agreement to the scaling. The slope of the line is $b = 4.1$, where b is a constant related to the amplitude of the singularity. Without a theory to which it can be compared, b does not give any insight into the velocity field of the fluid.

The impact experiment was repeated and its data were analyzed several times. The figures shown were from a typical dataset.

2.3. Conclusions

Two experiments that produce singularities on a fluid surface, the Faraday experiment and the impact experiment, were explored. A theory, motivated by the cylindrical shape of the pre-singularity surface

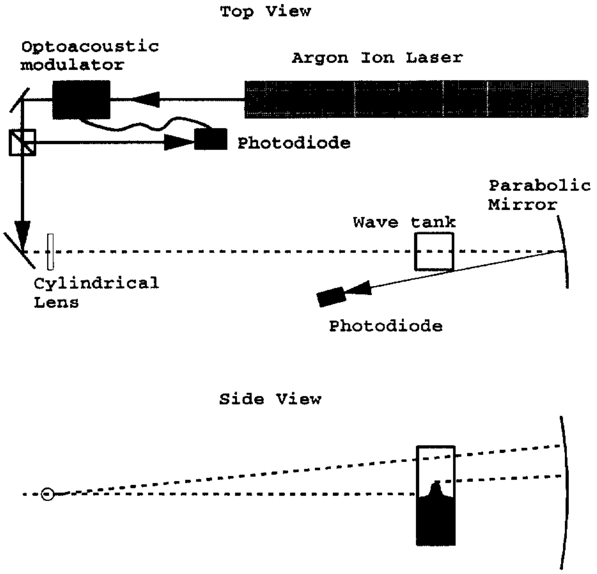

Fig. 12. Waveheight measurement technique. The curved wave surface scatters all laser light hitting it while the light propagating above it is unscattered. The unscattered light is collected by a parabolic mirror and focused on a photodiode. A computer monitors voltage on the photodiode, which can be directly related to the amplitude of light striking the photodiode, which in turn is a function of waveheight. This technique monitors the shadow of the wave along one cross-section.

depression in the Faraday experiment, predicted that the resulting shape of the singularity would grow according to the power law $z = btr^{-1/2}$. Investigation of the Faraday experiment resulted in a confirmation of the theory. Furthermore, information was derived about the velocity field of the fluid after the singularity occurred by comparing the experimental value for b to its predicted form. The impact experiment was found to produce a pre-singularity surface depression that was hourglass-shaped and thus different from the one produced by the Faraday experiment. This difference is thought to be responsible for the results that show a different growth of the singularity, $z = b(r/t)^{-2/5}$, but a growth that nonetheless is power-law in form.

3. Bifurcations leading to a singular wave state

In this section we explore the dynamics of the singular Faraday experiments using a novel laser diagnostic measuring system. This technique is used to measure waveheight. Fig. 12 shows how the measuring system functions. A uniform laser sheet is produced and aligned with the flat unshaken surface. As the waveheight grows above the flat surface, the light is scattered by the surface of the curved waves. The unscattered light above the maximum height of the waves is then collected in a photodiode detector using a concave mirror. The computer reads voltage signals from the detector that can be related back to the waveheight. Using this laser measurement technique, we gain a time series of maximum waveheight as a function of time. Fig. 13 shows some typical time-series data from the experiment. The square tank, 12 × 12 × 28 cm, contained 960 ml of a 92% glycerin–water solution. The (2, 2) Fourier mode of the tank was excited by a 7.40 Hz sinusoidal signal provided by an

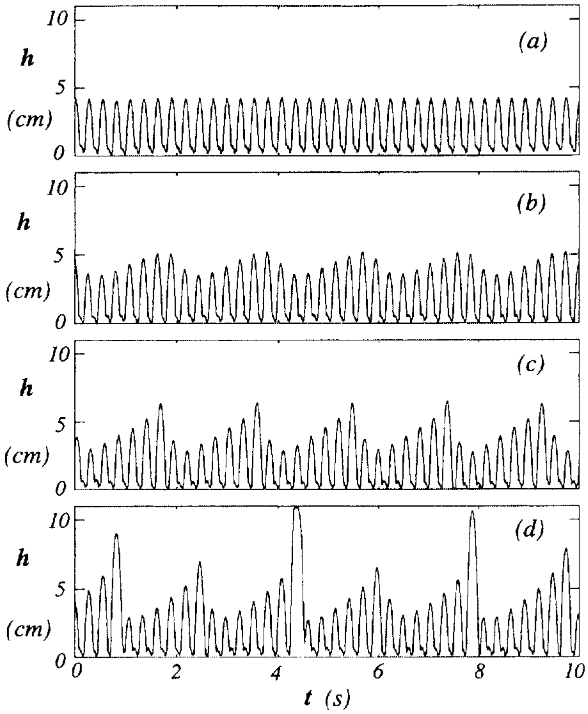

Fig. 13. Time series of the waveheight at a driving frequency of 7.40 Hz near the modulation threshold: (a) a periodic state (4.72 m/s^2), (b) a modulated state (4.98 m/s^2), (c) a period-7 state (5.08 m/s^2), and (d) an ejecting state (5.16 m/s^2). The flat top of the peak in (d) indicates the ejecting waveheight has exceeded the range of the diagnostic optics.

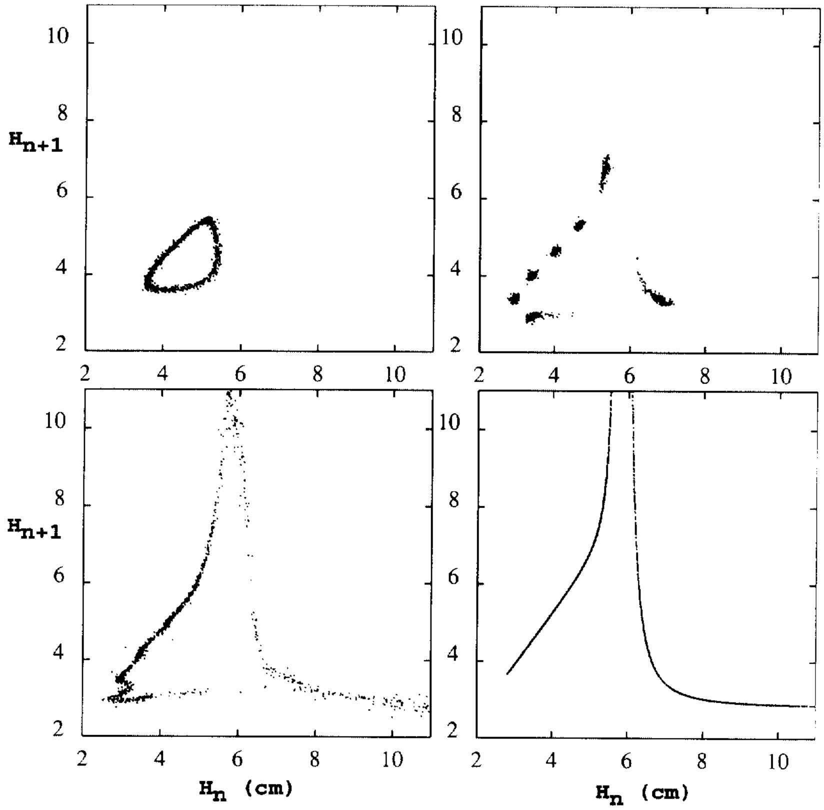

Fig. 14. Return maps showing (a) quasiperiodic motion, (b) period-7 motion, and (c) an aperiodic ejecting state as well as (d) model motion formed from local maximum values H_n from time series shown in the previous figure. Note that the instrument saturates at 11 cm and waves are observed in (c) with filaments that hit the roof of the container (28 mc, high). Those points between the two square brackets in (c) show entrainment and oscillations of air bubbles below the surface.

electro-magnetic linear actuator driven by a power amplifier.

The time series in Fig. 13 show typical dynamics of the system as we vary the acceleration of the tank. As we increase the acceleration, we see periodic states at 3.86 m/s^2 evolve to quasiperiodic states at 4.96 m/s^2, then to period-7 states at 5.06 m/s^2, and finally to broadband ejecting states at 5.10 m/s^2. If we continue to increase the acceleration, we find period-6 states and different chaotic states. Observations vary from relatively simple axisymmetric states to complicated swirling asymmetric states at higher acceleration.

Using the maximum height H_n of each wave, we construct a two-dimensional phase diagram $\{H_n, H_{n+1}\}$. These return maps are shown in Fig. 14, along with the return map for a system modeled after the experiment. We form a simple model of this observed return map for ejections:

$$H_{n+1} = \begin{cases} \gamma H_n + \dfrac{0.040 H_n}{(H_n - 0.48\lambda)^2}, & H_n < 0.48\lambda, \\ 2.8 + \dfrac{0.14 H_n}{(H_n - 0.48\lambda)^2}, & H_n > 0.48\lambda, \end{cases} \qquad (12)$$

where λ is the wavelength of the waves ($\lambda = 12$ cm here) and γ, a constant varying from 1 to 1.5 ($\gamma = 1.19$ for Fig. 14(c)). The location for the pole, at $H_n = 0.48\lambda$, is approximately independent of acceleration in the ejecting states and is likely a consequence of geometry alone. The linear growth term γ can be related back to the acceleration parameter by the following analysis. Distances in the map will grow as

$$\delta = \gamma^n \delta_0, \tag{13}$$

while distances in the flow will grow as

$$\delta = \delta_0 \exp(\sigma t). \tag{14}$$

The time in the flow is related to that of the map through the period and the number of maps, or

$$t = nT. \tag{15}$$

Following the method in Shi et al., the acceleration can be related to γ through σ, the growth rate of the wave, because

$$\sigma = -\sigma + \sqrt{(\kappa a)^2 - (\omega - \omega_0)^2} + k(a - a_0). \tag{16}$$

The linear term dominates, and we find

$$\gamma = \exp(Tk(a - a_0)), \tag{17}$$

which tells us how the growth rate is related to the tank acceleration. This equation allows us to compare the map and the physical system.

Fig. 14(a) shows the return map for the experiment at $a = 4.98\,\mathrm{m/s^2}$ displaying quasiperiodic motion; as acceleration is increased, the limit cycle deforms into a locked period-7 orbit (Fig. 14(b)). The map finally deforms and then forms folds for the ejecting state (Fig. 14(c)) upon further increase. This "singular" map has developed a region of large-amplitude excursions (here chopped above 11 cm due to limited height of the laser sheet), and this divergence corresponds to the filament tipped spikes observed in the experiment. Fig. 14(d) shows the return map generated by the model. The growth, decay, and singular characteristics of the wave states are represented quite nicely, but return mechanisms for wave states are not found in this model. This missing information is likely crucial to creating a more accurate model of the physical system.

Fig. 15 shows the bifurcation diagram of the model as a function of the growth parameter γ. The bifurcation diagram exhibits periodic windows along with chaotic regions, period doubling, and crisis phenomena. The bifurcation diagram undergoes reverse periodic window reduction similar to the experimentally observed sequence; the system may reach a period-7 state, exhibit chaos, and then exhibit a period-6 state as one increases the acceleration. This model shows periodic windows comparable to the experimentally observed sequence. However, the map does not capture the observed quasiperiodic to ejecting chaotic transition and is qualitatively similar only in the parameter region $1 < \gamma < 1.64$. A mapping of the form $H_{n+1} = g(H_n, H_{n-1})$ might better serve to model the return mechanisms.

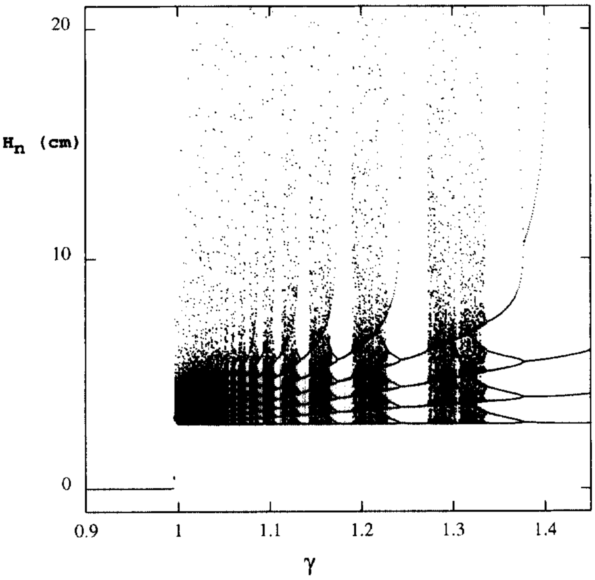

Fig. 15. The bifurcation diagram of the model as a function of γ. This diagram shows qualitatively similar windows as the physical data.

From the measurements of the waveheight, we construct a diagram, shown in Fig. 16, of the frequencies involved in the wave motion from power spectra of the wave height (Fig. 13) for both (a) the physical system and (b) the model. Both maps show period-6 and period-7 windows as well as aperiodic states. Very low noise levels in quasiperiodic and multiple-periodic states produce the blue background in the map. The spectra of the ejecting states have greater background in the map. The spectra of the ejecting states have greater background noise (the yellow background in

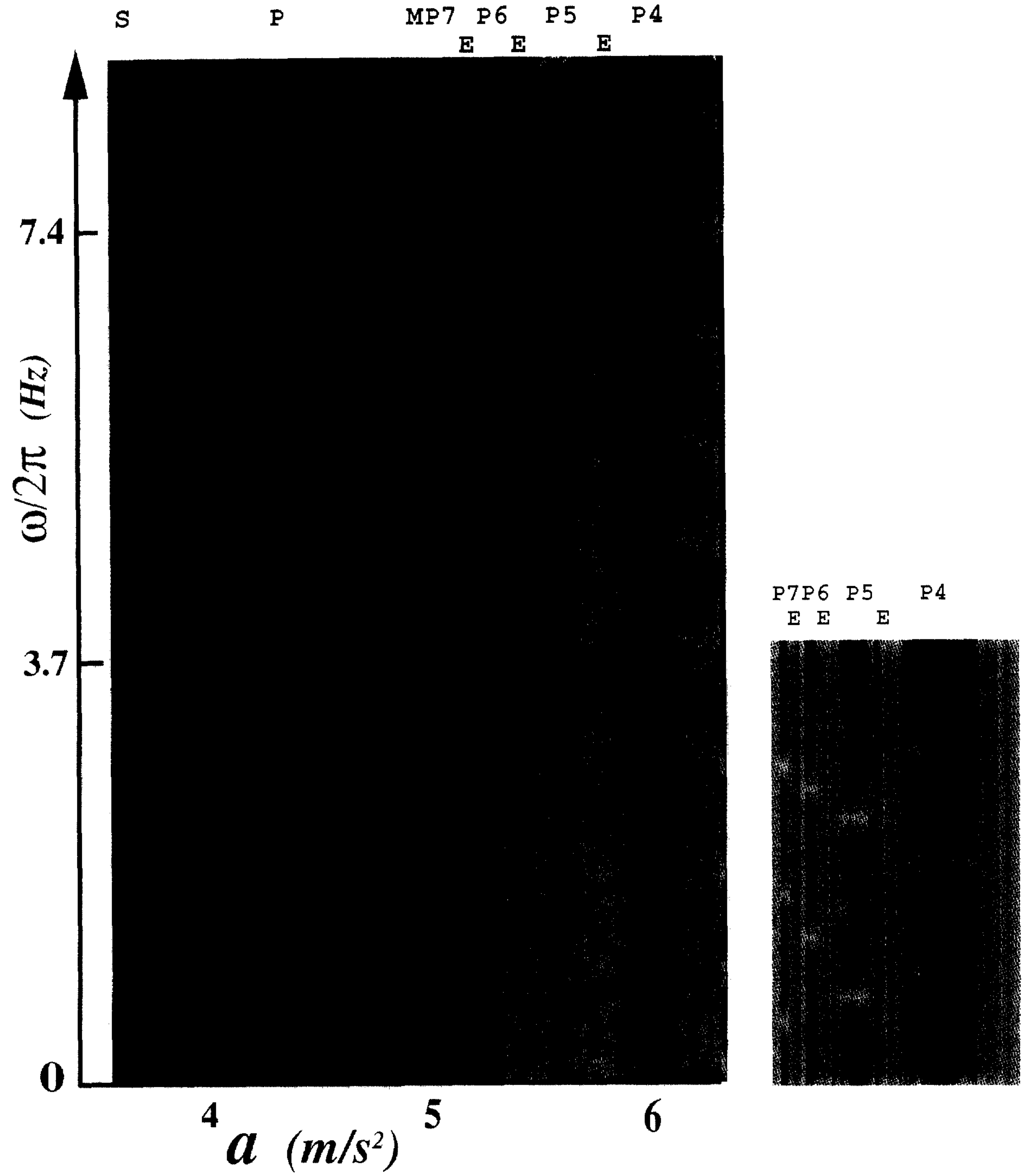

Fig. 16. A map of the power spectrum of waveheight as a function of the excitation acceleration and the spectrum frequency for both system and model, all with forcing frequency 7.40 Hz. Color represents the amplitude of the spectrum components, scaled from blue to red. (a) Each vertical strip represents one power spectrum of the time series of wave height as measured at a particular forcing level of the tank a_c. In (b) each vertical strip represents one power spectrum as measured at a_c levels as calculated from Eq. (17). Letters above denote stationary S, periodic P, modulated M, period-n Pn, and ejecting E wave states.

the map) in both the model and the system, implying aperiodic motion. Within the range $1 < \gamma < 1.64$, the model agrees relatively well with the experimental data, but outside this range, the model deviates substantially from the experimental data. The model does show many similarities with the physical system, including growth, decay, and singularities but lacks not only the clear transition from quasiperiodic to aperiodic states but also the return mechanisms in the return maps.

In summary, the Faraday system and model both exhibit singularities, and yet both have low-dimensional attractors associated with their dynamics. The simple model, although not exact, is qualitatively similar to the system with respect to growth, decay, and singular nature. The model fails to capture accurately the transition from quasiperiodic to aperiodic motion, but we are in the process of building better models for this system as well as examining Lyaponov exponents and entropies for both the system and model.

4. Viscous effects in droplet-ejecting capillary waves

This section examines the threshold for droplet ejection by turbulent surface waves produced by Faraday excitation. Faraday surface waves, their chaotic and turbulent bifurcation behavior, as well as a number of their transitions, have already been studied in depth [12–14,16,26,27]. This section describes capillary waves that experience a transition from a turbulent non-ejecting state to a turbulent ejecting state in a number of liquids with dissimilar fluid properties [21]. An example of an ejecting wave state in a viscous fluid can be seen in Fig. 17. This system has very turbulent behavior with a number of tall spikes that randomly eject droplets.

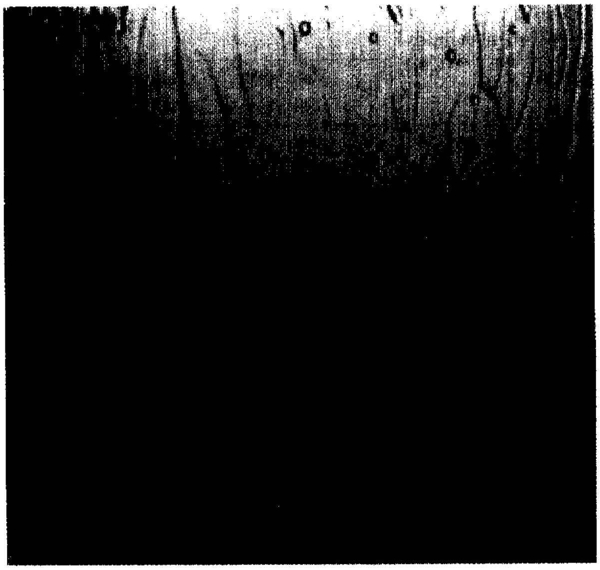

Fig. 17. Waves in an 80% glycerin–water ($\nu \simeq 0.43\,\mathrm{cm}^2\,\mathrm{s}$) solution exhibit random and turbulent behavior with a number of pronounced wave peaks. This system is forced at 20 Hz.

In capillary surface waves, the transition from a non-ejecting state to an ejecting state occurs when waves are forced to the point that the Rayleigh instability [25] breaks the wave peaks into droplets. This transition occurs according to the following pattern: First, the surface experiences several bifurcations from the initial flat surface [16,28,29]. Surface waves evolve from a periodic standing wave state with increased forcing and afterwards transform into an apeperiodic state. Enough forcing produces large-amplitude waves, frequently with elevated spikes that then break into droplets [19,21–24,30,31]. This transition is influenced by several factors: (1) the kinematic surface tension σ/ρ, (2) the kinematic viscosity of the fluid $\nu = \mu/\rho$, and (3) the applied forcing frequency ω_0, where ρ is the density of the liquid, σ is its interfacial surface tension, and μ is its Newtonian viscosity.

Droplet-ejection can occur over a wide range of fluid and forcing parameters and in states where either gravitational or capillary forces predominate. The distinction between these two types of waves, capillary and gravity, is determined by using the dispersion relationship for small-amplitude periodic waves of infinite depth [32],

$$\omega^2 = gk + \frac{\sigma}{\rho}k^3, \tag{18}$$

where ω is the angular frequency of the surface waves, g the local value of the gravitational acceleration, and k the wavenumber. Gravitational effects dominate at lesser values of k, and surface-tension effects dominate at higher values. Where the effects are equal, the

Table 2
Experimental fluids

Fluid	Viscosity (cm^2/s)	Kinematic surface tension (cm^2/s^2)
Distilled Water	0.01	72.0
Ethanol	0.012	28.8
20% Glycerin–water	0.0157	69.7
32% Glycerin–water	0.0226	67.3
44% Glycerin–water	0.0375	64.3
52% Glycerin–water	0.0548	62.5
58% Glycerin–water	0.0772	60.2
64% Glycerin–water	0.104	59.1
68% Glycerin–water	0.147	58.1
72% Glycerin–water	0.195	57.4
76% Glycerin–water	0.275	56.6
80% Glycerin–water	0.430	55.2
84% Glycerin–water	0.654	54.3
85% Glycerin–water	1.08	53.4

crossover wavenumber $k_c = \sqrt{g\rho/\sigma}$ determines the crossover frequency $\omega_c = g^{3/4}(\rho/\sigma)^{1/4}$. Our experiments focus on the region of higher frequency where capillary effects are the significant restoring forces ($\omega > \omega_c$). In these experiments, the consequences of the container geometry for the wave state have been minimized by working with capillary wavelengths much smaller than the container dimensions. Parametric excitation pushes energy primarily into waves of frequency $\omega = \omega_0/2$.

Our experiments determined the dependence of the threshold acceleration a on the frequency ω_0, the surface tension σ/ρ, and the viscosity of the fluid ν. Threshold accelerations for water, solutions of water and glycerin, and ethanol were measured according to the following procedure. Fluid with a depth of 10 cm was used in either a 13.5 cm diameter glass reaction flask or a 19.5 cm diameter cylindrical plastic container.[3] The fluids used in this experiment are listed in Table 2.

The container was then mounted on a TA100-20 Unholtz-Dickie Electromagnetic shaker, which supplies up to 1100 N of force. A sinusoidal signal was supplied to the shaker by a function generator and amplifier. Applied acceleration was measured with an accelerometer mounted on the armature of the shaker. Either a FFT or a lock in amplifier was used to process the accelerometer signal. Temperature was controlled by running fluid from a bath of constant temperature under an aluminum plate which served as the bottom of the tank. The droplets were visually detected. Since a critical slowing of droplet production appears near the threshold, the criterion developed and used for onset of droplet ejection was two droplets detected within a 10 s period. This threshold criterion introduces 2–3% error to the data. Fig. 18 represents the viscous dependence of the threshold acceleration for seven different fluids.

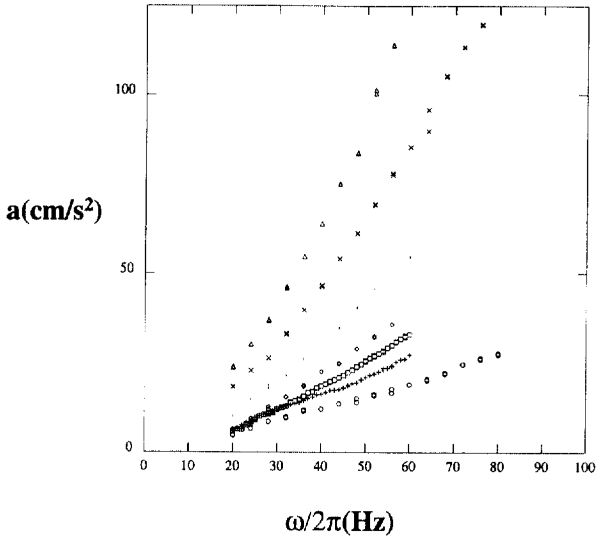

Fig. 18. The threshold accelerations for ethanol (○), water (+), and five glycerin–water solutions (52% □, 68% □, 76% I, 84% X, 85% Δ). The viscosities of these fluids vary over two orders of magnitude (0.01–1.08 cm^2/s) while the surface tension has a range of 22.75–72 cm^3/s^2.

In order to determine the functional form of the threshold acceleration, the experimental threshold acceleration a is plotted against angular forcing frequency ω_0, scaled with the fluid parameters of kinetic surface tension σ/ρ and kinetic viscosity ν. Fig. 19 illustrates this plot. Our definition of a non-dimensional

---

[3] Low frequency states where the wavelengths are non-negligible when compared to container dimensions have waves which are influenced by the geometry of the container. Low frequency states will exhibit approximately stationary ejecting waves as well as periodic ejecting states in certain circumstances. The bottom boundary contribution to the surface wave state is minimized by using this depth ($d > 10\gamma$).

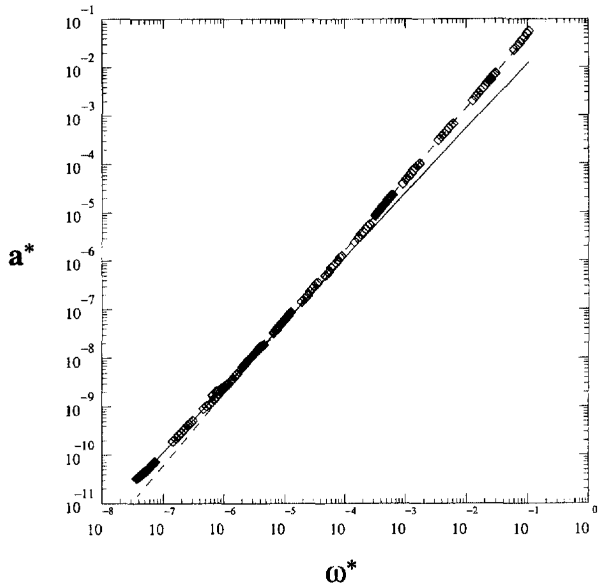

Fig. 19. The threshold acceleration $a^* = a\nu^3/(\sigma/\rho)^4$ and forcing frequency $\omega^* = \omega_0\nu^2/(\sigma/\rho)^3$ are scaled with the fluid parameters of viscosity and surface tension. The strength of this non-dimensionalization is shown by the collapse of all of the data. The non-dimensionalized acceleration $a^* = a\nu^3/(\sigma/\rho)^4$ exhibits a transition between low- and high-viscosity behavior. At low viscosities ($\omega^* < 10^{-5}$), there is an $\omega_0^{4/3}$ dependence, illustrated by the solid line. In the higher viscosity region ($\omega^* > 10^{-5}$), the threshold acceleration exhibits an $\omega_0^{3/2}$ dependence, as shown by the dashed line.

frequency is[4]

$$\omega^* = \frac{\omega_0\nu^3}{(\sigma/\rho)^2} \tag{19}$$

and of a non-dimensional acceleration (see footnote 4) is

$$a^* = \frac{a\nu^4}{(\sigma/\rho)^3}. \tag{20}$$

These scaled quantities cross over each other at about $\omega^* \simeq 10^{-5}$, evident in Fig. 20. For $\omega^* \ll 10^{-5}$, the angular frequency dependence $a^* \sim (\omega^*)^{4/3}$ (regression yields $(\omega^*)^{1.337}$) is observed, while for $\omega^* \gg 10^{-5}$, a dependence of $a^* \sim (\omega^*)^{3/2}$ (regression yields $(\omega^*)^{1.476}$) is seen. This crossover leads to two different functional forms for the threshold acceleration: (1) for fluid of low viscosity, where surface tension effects predominate, the threshold acceleration a is given by

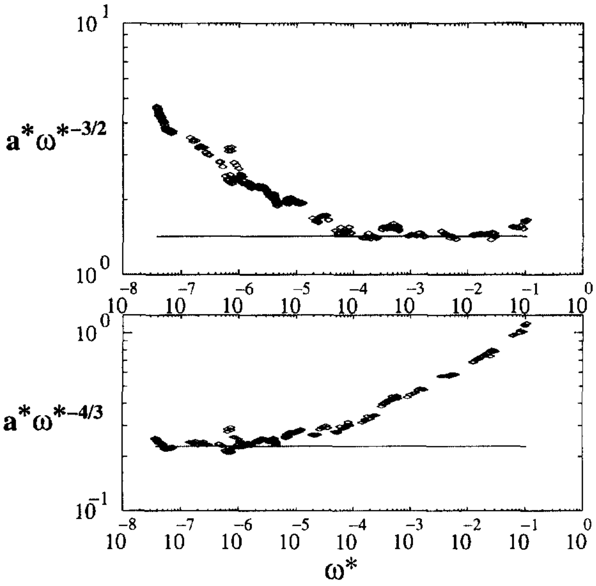

Fig. 20. The transition between low- and high-viscosity behavior is shown by scaling the non-dimensionalized threshold acceleration with $(\omega^*)^{-3/2}$ and $(\omega^*)^{-4/3}$.

$$a \approx 0.261 \left(\frac{\sigma}{\rho}\right)^{1/3} \omega_0^{4/3} \tag{21}$$

or (2) for fluids where viscous effects predominate, the functional form for a is

$$a \approx 1.306\nu^{1/2}\omega_0^{3/2}. \tag{22}$$

Coefficients were determined by linear regression. Both acceleration regions can be described by power laws based on the same model for both low- and high-viscosity systems. According to this model, ejections occur, as the forcing is increased, when the ratio of the waveheight h to the wavelength λ approaches unity:

$$h \sim \lambda. \tag{23}$$

Analytical work done on waves formed in other systems supports this assumption. Limiting waveheight and wavelength ratios, for both gravity and capillary traveling waves, have been determined [33,34]. The

---

[4] The simplest free surface response to vertical excitation is at one-half the excitation frequency, so the crossover excitation frequency is twice ω_0.

waveheight/wavelength ratio is $s = h/\lambda = 0.14$ for gravity waves and $s = 0.731$ for capillary waves. If h/λ exceeds the above ratio for gravity waves, local accelerations on the crest of the wave diverge, and waves break. For periodic capillary waves, heights h must be less than 0.731λ. The parametric solution will intersect itself otherwise. This corresponds to the impact of two diverging vertical surfaces in the wave, when jet formation [35,36] or air entrainment may occur.

The motion of the tank can be described as simple harmonic:

$$z = A \sin \omega_0 t, \tag{24}$$

where z is the vertical displacement of the tank, A is the peak displacement, and $\omega_0 = 2\omega$ is the angular velocity of the external forcing. Where low-viscosity effects predominate, the assumption will remain that waveheight scales as the amplitude of the external forcing $h \alpha A$. Restated in terms of the applied acceleration, this is

$$h \alpha \frac{a}{\omega_0^2}. \tag{25}$$

Our experimental observations confirm that for capillary waves $h \simeq 47a/\omega_0^2$.[5] This assumption and the dispersion relation for small-amplitude capillary waves determine that the threshold acceleration for droplet production in lowviscosity fluids scales as $a \sim h\omega_0^2 \sim \lambda\omega_0^2$, or

$$a = c_1 \omega_0^{4/3} \left(\frac{\sigma}{\rho}\right)^{1/3}, \tag{26}$$

where c_1 is some constant. Therefore, consistent with observation, the threshold for low-viscosity fluids depends on only surface tension and forcing frequency.[6]

The waveheight is controlled by the balance of power input and viscous dissipation in higher viscosity fluids. The dissipation of viscous energy per unit mass is expressed as

$$\epsilon = \sum_{i,j} \frac{\nu}{2} \left(\frac{\partial v_i}{\partial x_j} + \frac{\partial v_j}{\partial x_i} \right)^2, \tag{27}$$

where $\partial v_i / \partial x_j$ is the rate of strain components within the fluid. Energy dissipation scales, therefore, as

$$\epsilon = \nu \left(\frac{v}{l}\right)^2, \tag{28}$$

where v is the characteristic length of the ejecting surface waves and l is their velocity scales. With the maximum velocity $|v_{\max}| = h\omega$ as the characteristic velocity and the wavelength λ as the characteristic length, the power dissipation is now

$$\epsilon \simeq \nu \left(\frac{v_{\max}}{\lambda}\right)^2 = \nu \left(\frac{h\omega}{\lambda}\right)^2. \tag{29}$$

The injected power can be expressed in terms of the force and velocity of the tank $P = Fv$, where $v = a/\omega_0$, the peak velocity of the tank, and $F = ma$, where m is the mass of the fluid and a is the peak applied acceleration. The injected power per unit mass $p = P/m$ is thus

$$p \sim \frac{a^2}{\omega_0}. \tag{30}$$

The following relationship is produced by equating the injected power with the viscous dissipated energy and using the hypothesis $h \sim \lambda$:

$$a = c_2 \omega_0^{3/2} \nu^{1/2}. \tag{31}$$

Although the value for surface tension occurs in the wavelength in this calculation, it no longer appears in the expression for the threshold acceleration for viscous liquids, as corroborated by the $a^* \sim (\omega^*)^{3/2}$ dependence of the experimental observations.[7]

To summarize, viscous effects on the threshold for droplet ejection in capillary Faraday waves have been

---

[5] This nondimensionalization is arrived at by taking a nondimensional acceleration $a^* = a\sqrt{\sigma l^2/\rho}$ and using the corresponding wavelength $\lambda = l$ from the capillary dispersion relation.

[6] Dimensional analysis can also be used to derive expressions for the threshold acceleration. Surface tension σ/ρ and frequency ω can combine to an acceleration in only one way: $a \, \alpha (\sigma/\rho)^{1/3}\omega^{4/3}$.

[7] An acceleration can only be formed from $\omega^{3/2}$, ν, and σ/ρ if $a = \omega^{3/2}\nu^{1/2}$.

investigated for water, ethanol, and glycerin–water solutions. The observed viscous effects have been identified by first varying the fluid properties and the forcing parameters and then ascertaining the threshold acceleration of several fluids. Not only has a transition in behavior at the threshold been discovered, but a simple scaling theory has also produced relationships for both behavior regimes and has supported our experimental observations. Subsequent analysis of the droplet-ejecting Faraday waves will include a statistical description of the droplet rates near threshold.

Acknowledgements

The authors would like to express their gratitude to the following people: R. Behringer, M.P. Brenner, M. Brown, R. DuVarney W.S. Edwards, C. Doering, D. Lohse, S.E. Ralph, R. Roy, M. Steffen, H.L. Swinney, and B. Zeff. This research was funded in part by the Emory University Research Committee and by NSF DMR-9896037. Dr. Daniel Perry Lathrop is a Cottrell Scholar of the Research Corporation.

References

[1] K.R. Sreenivasan, C. Meneveau, Phys. Rev. A 38 (1988) 6287.
[2] R.T. Knapp, J.W. Dailey, F.G. Hammitt, Cavitation, McGraw-Hill, New York, 1970.
[3] D.F. Gaitan, L.A. Crum, C.C. Church, R.A. Roy, J. Acoust. Soc. Am. 91 (6) (1992) 3166.
[4] Y.R. Shen, The Principles of Nonlinear Optics, Wiley, New York, 1984.
[5] B.P. Luce, C.R. Doering, Phys. Lett. A 178 (1993) 92.
[6] S. Weinberg, Gravitation and Cosmology, Wiley, New York, 1972.
[7] J. Eggers, Phys. Rev. Lett. 71 (1993) 3458.
[8] J. Eggers, Phys. Fluids 7 (1995) 941.
[9] A.C. Newell, V.E. Zakharov, Phys. Rev. Lett. 69 (1992) 1149.
[10] E.A. Kuznetsov, M.D. Spector, V.E. Zakharov, Phys. Rev. E 49 (1994) 1283.
[11] M. Faraday, Phil. Trans. R. Soc. London 121 (1831) 299.
[12] T.B. Benjamin, F. Ursell, Proc. R. Soc. London Ser. A 225 (1954) 505.
[13] S. Douady, J. Fluid Mech. 221 (1990) 383.
[14] S. Cilberto, S. Douady, S. Fauve, Europhysics Letters 15 (1) (1991) 23.
[15] W.S. Edwards, S. Fauve, Phys. Rev E 47 (1993) R788.
[16] N.B. Tufillaro, R. Ramshankar, J.P. Gollub, Phys. Rev. Lett. 62 (1989) 422.
[17] J. Miles, D. Henderson, Annu. Rev. Fluid Mech. 22 (1990) 143.
[18] O.N. Mesquita, S. Kane, J.P. Gollub, Phys. Rev. A 45 (1992) 3700.
[19] Jens Eggers, Todd F. Dupont, J. Fluid Mech. 262 (1994) 205.
[20] V.E. Zakharov, in: M.L. Banner, R.H.J. Grimshaw (Eds.), Breaking Waves, IUTAM Symposium 1991, Springer, Berlin, 1992.
[21] C.L. Goodridge, W. Tao Shi, D.P. Lathrop, Phys. Rev. Lett. 76 (1996) 1824.
[22] M.S. Longuet-Higgins, H. Oguz, J. Fluid Mech. 290 (1995) 183.
[23] M.P. Brenner, X.D. Shi, S.R. Nagel, Phys. Rev. Lett. 73 (1994) 3391.
[24] M.S. Longuet-Higgins, J. Fluid Mech. 127 (1983) 103.
[25] S. Chandrasekhar, Hydrodynamic and Hydromagnetic Stability, Dover, New York, 1981.
[26] B.J. Gluckman, C.B. Arnold, J.P. Gollub, Phys. Rev. E 51 (1995) 1128.
[27] S.P. Decent, A.D.D. Craik, J. Fluid Mech. 293 (1995) 237.
[28] A.B. Ezerskii, P.I. Korotin, M.I. Rabinovich, JETP Lett. 41 (1985) 157.
[29] S. Cilberto, J. Gollub, J. Fluid Mech. 158 (1985) 381.
[30] M. Tjahjadi, H.A. Stone, J.M. Ottino, J. Fluid Mech. 243 (1992) 297.
[31] W. Tao Shi, C.L. Goodridge, D.P. Lathrop, Phys. Rev. E, to appear.
[32] L.D. Landau, E.M. Lifshitz, Fluid Mechanics, Pergamon Press, New York, 1987.
[33] J.H. Michell, Philos. Mag. 36 (1893) 430.
[34] G.D. Crapper, J. Fluid Mech. 2 (1957) 532.
[35] E. Ott, Phys. Rev. Lett. 29 (1972) 1429.
[36] J.M. Walsh, R.G. Shreffler, F.J. Willig, J. Appl. Phy. 24 (1953) 349.